Compositionally Tuned Trimetallic Thiospinel Catalysts for Enhanced Electrosynthesis of Hydrogen Peroxide and Built-In Hydroxyl Radical Generation

R. Dominic Ross,[1] *Hongyuan Sheng,*[1] *Aditya Parihar,*[1] *Jinzhen Huang,*[1,2] *and Song Jin*[*,1]

[1]Department of Chemistry, University of Wisconsin–Madison, 1101 University Avenue, Madison, Wisconsin 53706, United States

[2]Center for Composite Materials and Structures, Harbin Institute of Technology, Harbin 150001, China

ABSTRACT

On-site electrochemical production of hydrogen peroxide (H_2O_2), an oxidant and disinfectant with growing demand, could be realized through the selective two-electron oxygen reduction reaction ($2e^-$ ORR), but the widespread adoption of this method depends on robust and efficient electrocatalysts. Current catalysts have been limited by cost or toxicity and lack well-defined structures that can facilitate systematic tuning of activity and selectivity. Here, we demonstrate a series of $CuCo_{2-x}Ni_xS_4$ ($0 \leqslant x \leqslant 1.2$) thiospinel catalysts for $2e^-$ ORR with variable compositions that can be synthesized via hydrothermal conversion. Rotating ring disk electrode measurements show that these catalysts have high selectivity for $2e^-$ ORR (>60%), and that their activity can be improved by increasing the nickel content without compromising selectivity. An acid treatment step is critical prior to employing the optimized $CuCo_{0.8}Ni_{1.2}S_4$ catalyst for bulk electrosynthesis of H_2O_2 in 0.05 M H_2SO_4 solution. Various structural analyses, including synchrotron X-ray spectroscopy, confirm that the catalysts retain the spinel structure after acid treatment and H_2O_2 electrosynthesis. The acid treatment likely leaches the soluble copper species from the as-synthesized catalysts that would catalyze an electro-Fenton process to consume H_2O_2 and generate hydroxyl radicals and therefore prevent the accumulation of H_2O_2. This work demonstrates a general strategy for systematic tuning of metal compound catalysts for practical H_2O_2 electrosynthesis and facile generation of hydroxyl radicals.

KEYWORDS

oxygen reduction reaction; selective electrocatalysis; thiospinel; hydrogen peroxide, electro-Fenton; earth-abundant

INTRODUCTION

Hydrogen peroxide (H_2O_2) is a useful oxidant and disinfectant with diverse industrial and everyday applications, with an increasing global demand that exceeds 5 million tons per year.[1-4] The production of H_2O_2 mostly relies on the anthraquinone process, which requires noble metal catalysts, hydrogen gas, and energy-intensive distillation steps that generally take place in centralized chemical plants.[5, 6] Even though most downstream uses of H_2O_2 require a concentration of as little as 0.1 wt%,[7] usually concentrated solutions of H_2O_2 exceeding 70 wt% are produced by the anthraquinone process and transported, which can be hazardous. Direct electrosynthesis of H_2O_2 via the two-electron oxygen reduction reaction ($2e^-$ ORR) could present a cheaper, safer, and more environmentally conscious approach to producing H_2O_2 on-demand at the point of use.

However, the widespread adoption of H_2O_2 electrosynthesis has been hindered by the lack of active and inexpensive catalysts that are selective for $2e^-$ ORR rather than the four-electron ORR process towards H_2O, especially in acidic or neutral solutions.[8, 9] To date, the development of $2e^-$ ORR catalysts, especially in acidic solution, has focused on various ways to disperse active sites, which can increase the barrier to further reduction to H_2O after the initial binding of the OOH* intermediate species by preventing scission of the O-O bond.[1] However, many of these catalysts utilize noble metals[10] and/or toxic elements.[10, 11] Carbon-based catalysts[12-14] have been demonstrated as promising earth-abundant catalysts with high selectivity towards $2e^-$ ORR although many are more active in alkaline media,[15] in which H_2O_2 is less stable.[16] Due to the stability of H_2O_2 in acidic media and due to the high concentration of protons that facilitate ORR compared to neutral media, $2e^-$ ORR in acidic media ($O_2 + 2H^+ + 2e^- \rightarrow H_2O_2$, $E^\circ = 0.69$ V vs. RHE) could be more promising. Single atom catalysts (SACs) more recently emerged as promising $2e^-$ ORR[17-21] catalysts with natural active site dispersity that can be active in acidic media, although

the lack of well-defined periodic structures in SACs and their sensitivity to the environment around the active site[18, 22] limit their potential for systematic tuning improvements. The few demonstrated examples of compositional tuning typically resulted in an increasing activity with decreasing selectivity, or vice-versa.[19, 23]

Along with the development of $2e^-$ ORR SACs, transition-metal compounds such as CoS_2,[24, 25] $CoSe_2$,[26] and other binary metal compounds[27, 28] have been demonstrated to be selective and active catalysts that are practical for H_2O_2 electrosynthesis in acidic media. Further tuning of the catalytic activity and selectivity could be anticipated when more complex metal compound catalysts beyond binary compounds are studied. Spinels, with a general formula of AB_2X_4 (A, B = metal ions, X = chalcogens),[29] could be a promising class of catalyst materials for the selective $2e^-$ ORR as they: (i) provide intrinsic metal ion separation within the relatively inert chalcogen matrix and (ii) allow for the inclusion of two or more metal elements in different coordination environments within a well-defined crystal structure. However, spinels present a challenge due to their complex metal site mixing.[30] Even though normal spinels are typically defined as ${A^{II}}_{T_d}(B^{III}, B^{III})_{O_h}X_4$ and inverse spinels termed as ${B^{III}}_{T_d}(A^{II}, B^{III})_{O_h}X_4$ (T_d = tetrahedral metal sites, O_h = octahedral metal sites), the actual structures are often much more complex due to the mixing of metal sites with fractional site distributions and varying metal oxidation states.[29, 31-33] The metal oxidation states and site mixing within spinels are known to be synthesis-dependent,[30, 34] therefore, the properties of spinels are highly tunable but their structures are difficult to characterize. Several studies have shown improved oxygen evolution electrocatalytic properties in spinel oxides by tuning the composition of tetrahedral[35] or octahedral[36, 37] sites. Additionally, the thiospinel $CuCo_2S_4$ was reported as an electrocatalyst for the alkaline ORR.[38] The octahedral metal sites are expected to be the more active sites for ORR and Cu has a strong preference for tetrahedral

sites in thiospinels, so tetrahedral Cu can act as a further dilutant of the active octahedral sites to ensure $2e^-$ selectivity. Since the ionic radii of Co and Ni are similar,[39] we hypothesize that one possible way to enhance the ORR activity of $CuCo_2S_4$ could be substituting some Co for Ni, while keeping the likely inert Cu tetrahedral site constant. Substitution of Ni into some of the metal sites in $CuCo_2S_4$ has been reported in the mineral literature[40, 41] but reports on the syntheses of a trimetallic Cu-Co-Ni thiospinel have been limited.[42] Given the recent reports of $2e^-$ ORR catalysts with Co active sites,[18, 24, 26] systematically modifying the likely octahedral Co active site[43] of the thiospinel offers an opportunity for studying how compositional changes can modify both activity and selectivity for $2e^-$ ORR.

Here, we present a series of mixed trimetallic $CuCo_{2-x}Ni_xS_4$ ($0 \leqslant x \leqslant 1.2$) thiospinels based on Cu, Co and Ni that are hydrothermally synthesized and demonstrate the ability to increase the ORR activity without compromising its high $2e^-$ ORR selectivity in acidic media. An additional acid treatment of the as-synthesized catalysts is crucial for bulk electrosynthesis of H_2O_2 while still maintaining the spinel structure. Without such treatment, an electro-Fenton process is catalyzed by the soluble copper species leached from as-synthesized catalysts to generate hydroxyl radicals. This work presents thiospinels as a previously unexplored class of catalyst materials for selective H_2O_2 electrosynthesis and subsequent generation of hydroxyl radicals and serves as a case study to demonstrate a general strategy for improving complex metal chalcogenide catalysts through compositional tuning and subsequent treatment.

RESULTS AND DISCUSSION

Synthesis and Characterization of Trimetallic Thiospinel Catalysts. We synthesized mixed-metal-site trimetallic thiospinel catalyst powders with the general formula $CuCo_{2-x}Ni_xS_4$ (CCNS) by first synthesizing trimetallic metal hydroxide precursors (Scheme 1, Step I) and then converting

them using a hydrothermal sulfidation process with an excess of sodium sulfide to obtain CCNS (Scheme 1, Step II, see Supporting Information for details). The general process was modified from previously reported synthesis procedures for $CuCo_2S_4$.[44, 45] Assuming primarily octahedral substitution of Co by Ni, nominal nickel loadings were increased stoichiometrically while cobalt loadings were decreased proportionally. The four synthesized CCNS samples with varying Ni substitution are defined by the total amount of formula nickel equivalents added as *x*, ranging from 0 to 1.2 for these four $CuCo_{2-x}Ni_xS_4$ samples (x = 0, 0.4, 0.8, 1.2).

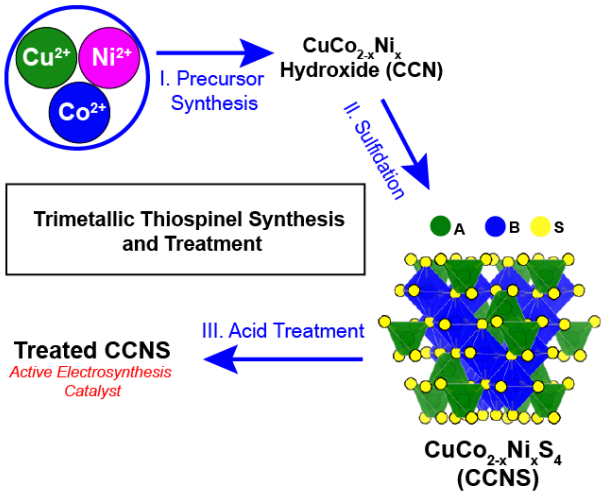

Scheme 1. Synthesis process of the active $CuCo_{2-x}Ni_xS_4$ catalysts: I) Hydrothermal synthesis of initial mixed $CuCo_{2-x}Ni_x$ metal hydroxide precursor, termed CCN; II) hydrothermal sulfidation of CCN to a single-phase $CuCo_{2-x}Ni_xS_4$ thiospinel, termed CCNS; III) room temperature acid treatment of CCNS in H_2SO_4 to yield the final treated CCNS phase for bulk electrosynthesis of H_2O_2.

Scanning electron microscopy energy dispersive X-ray spectroscopy (SEM-EDS) and X-ray photoelectron spectroscopy (XPS) measurements of these CCNS samples reveal excellent agreement between the percentage of Ni and Co elements present in the powders and the nominal loading of Ni and Co into the precursors (Figure 1a, Table S1, and Table S2). Powder X-ray

diffraction (PXRD) patterns of the as-prepared CCNS samples (Figure 1b), showed peaks all matching closely with the standard pattern for $CuCo_2S_4$ (the $x = 0$ phase), and thus confirmed the spinel phases. There is a small, but systematic, peak shift to higher 2θ as the Ni substitution increases, due to the difference in atomic radii between Ni and Co. Further increasing the nominal loading of Ni to $x = 1.4$ yielded a dominant non-spinel phase (Figure S1), suggesting that a $CuNi_2S_4$ phase (the would be "$x = 2$ phase") is not attainable, consistent with known mineral compositions.[40, 41] The successful incorporation of Ni in CCNS ($x \leqslant 1.2$) is further confirmed by Raman spectroscopy. Raman peaks for the CCNS $x = 0$ phase matches the known peaks that fingerprint the $CuCo_2S_4$ phase,[46] and the major peak displays a systematic red shift and decrease in intensity as the Ni substitution increases (Figure 1c and Figure S2). XPS reveals little change in the peak positions of Cu, Co, and S, but some change in the binding energy of the Ni peaks (Figure S3). SEM-EDS elemental mapping shows strong spatial correlation between the elemental signals (Figure S4) further suggesting a monophasic spinel even at the highest Ni substitution level. SEM images of CCNS (Figure S5) reveal a high-surface area morphology for all four samples.

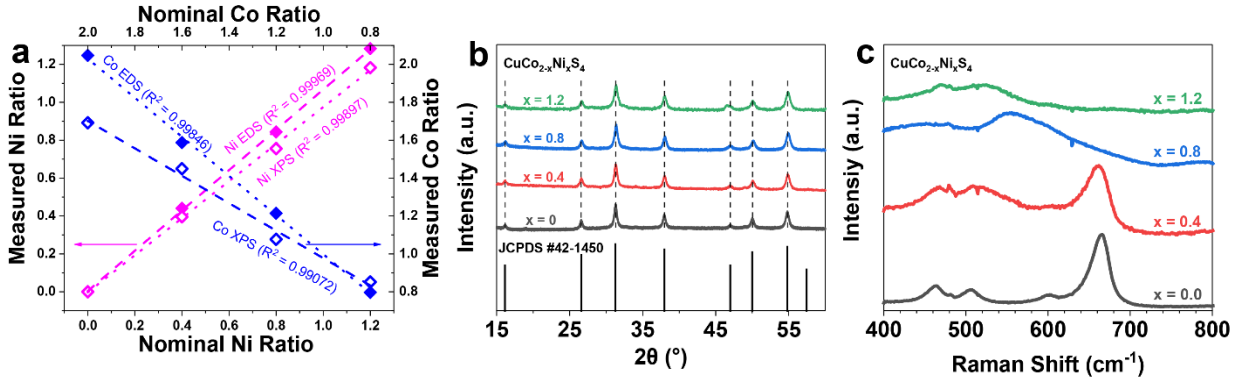

Figure 1. Structural characterization of as-synthesized nanostructured CCNS ($x = 0$, 0.4, 0.8, and 1.2) catalysts. a) Elemental compositions of CCNS powders by SEM-EDS (filled diamonds) and XPS (empty diamonds) as a function of the nominal loading of Co and Ni. b) Powder X-ray

diffraction patterns of CCNS powders in comparison with the standard pattern of $CuCo_2S_4$ (JCPDS #42-1450). c) Raman spectra of CCNS powders.

Selectivity and Activity of Trimetallic Thiospinel Catalysts for ORR. We then used a rotating ring-disk electrode (RRDE) to evaluate the catalytic activity and selectivity towards $2e^-$ ORR on this series of as-synthesized catalysts to study the effect of increasing Ni substitution. The RRDE was first calibrated using a ferri-/ferrocyanide redox couple and determined to have a collection efficiency of 39% (Figure S6). The uncompensated resistance of each measurement was calibrated by electrochemical impedance spectroscopy (Figure S7). The CCNS powders were dispersed in a Nafion-containing solution then drop-casted onto the glassy carbon disk of the RRDE. Then, ORR was measured on the disk electrode in O_2-saturated 0.05 M H_2SO_4 while the Pt ring electrode was held at a constant potential to selectively detect the production of H_2O_2 at the diffusion limit (see the Supporting Information for details). A constant mass loading of 159 $\mu g/cm^2$ was used for all four samples, which was chosen based on the mass loading-activity/selectivity tradeoff of $CuCo_2S_4$ (Figure S8). The observed mass loading trend follows previous studies on the impact of catalyst loading on H_2O_2 selectivity.[24, 26, 47]

All four CCNS catalysts were found to be selective (~60-70%) toward $2e^-$ ORR across the measured potential range (0.6 V to 0.25 V vs. RHE), with little variation of selectivity as the Ni substitution level is varied (Figure 2 and Figure S9). The CCNS $x = 1.2$ exhibits similar ring current and selectivity to the CoS_2 catalyst measured at 637 $\mu g_{catalyst}/cm^2$ (305 $\mu g_{Co}/cm^2$),[24] but with a less severe drop in selectivity at higher overpotentials. However, the mass activity increases as evidenced by the increasing current density for both the disk and ring electrodes – the ring current density increase additionally suggests an overall higher amount of H_2O_2 produced. The similarity of the measured double-layer-capacitance (Figure S10 and Figure S11) across all samples suggests

that this activity increase was not an effect of increasing surface area. Koutecky-Levich (K-L) analysis of the disk current showed modest agreement with the RRDE data at high overpotential (Figure S12, Supplementary Note 1 and Table S3). K-L analysis of the ring current also allows for calculation of the kinetic current density towards H_2O_2 production (see Supporting Information for details), which allows for a performance comparison to other previously reported catalysts in acidic media (Figure S13).

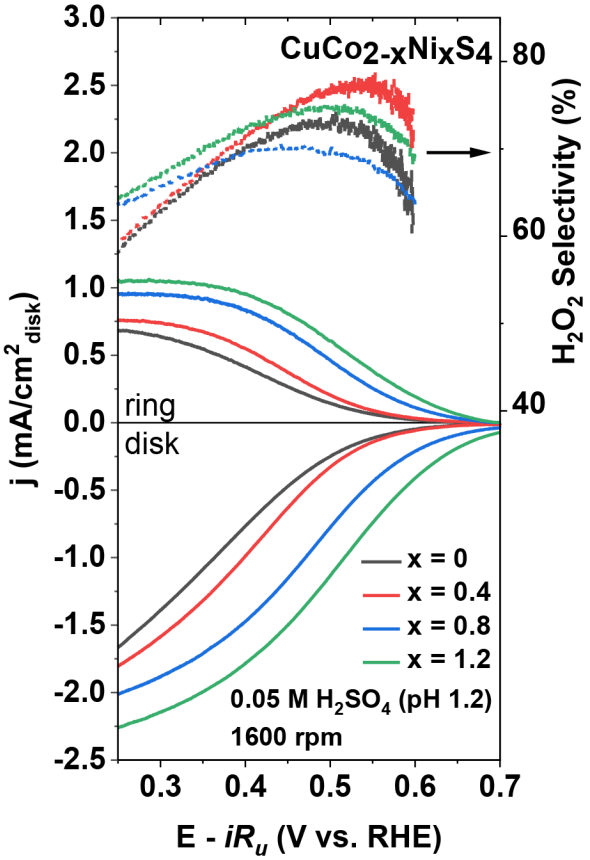

Figure 2. RRDE voltammograms measured at 1600 rpm in O_2-saturated 0.05 M H_2SO_4 (pH = 1.2) and the corresponding H_2O_2 selectivity of various $CuCo_{2-x}Ni_xS_4$ catalysts.

Electrosynthesis of H_2O_2 Using Optimized Trimetallic $CuCo_{0.8}Ni_{1.2}S_4$ Catalyst. For the bulk electrosynthesis of H_2O_2, the CCNS catalysts were synthesized directly onto carbon fiber paper

(CFP) to maximize the electrode surface area. The CCNS/CFP was subsequently cut to have a solution accessible surface area of ~1cm^2 (Figure S14). Furthermore, before electrolysis we performed an acid treatment step where the CCNS/CFP was soaked in 0.05 M H_2SO_4 for three hours (Scheme 1, Step III). The role of the acid treatment is to remove the easily leached copper species from the sample and to guarantee H_2O_2 accumulation (see further discussion later). A constant potential of 0.25 V vs. RHE was applied to the treated CCNS (x = 1.2)/CFP in O_2-saturated 0.05 M H_2SO_4 and the current was measured (Figure 3a) while periodically sampling aliquots of the electrolyte for spectroscopic chemical detection of the H_2O_2 product (Figure S15, see experimental details in Supporting Information). The concentration of H_2O_2 was found to reach 84 ppm before beginning to degrade (Figure 3b), which corresponded to a peak H_2O_2 yield of 11.1 μmol (Figure 3c). Then the production of H_2O_2 was limited by a low selectivity which decreased over the course of the measurement (Figure 3d), likely due to an increasing rate of H_2O_2 reduction to water caused by the accumulation of H_2O_2.

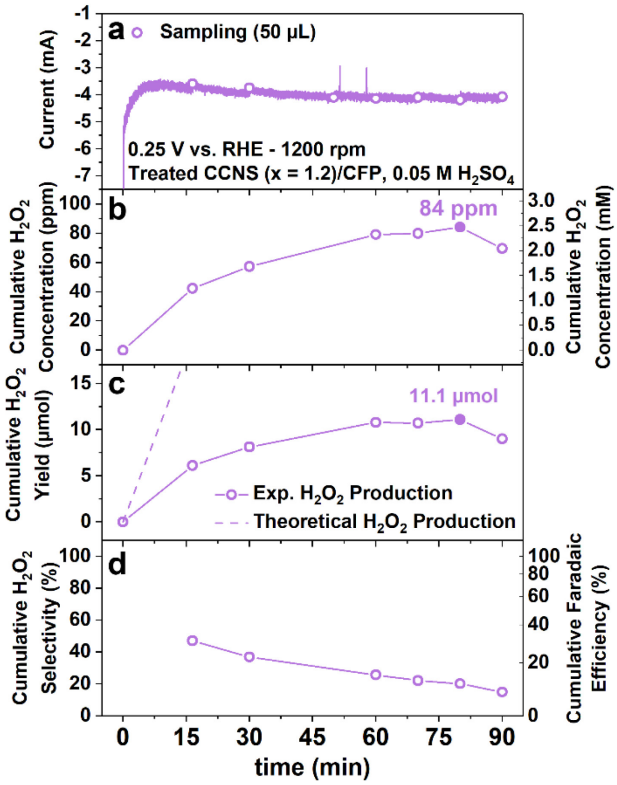

Figure 3. Bulk electrosynthesis and chemical detection of H_2O_2 produced on acid treated CCNS (x = 1.2)/CFP. a) Chronoamperometry curve of treated CCNS (x = 1.2)/CFP at 0.25 V vs. RHE in O_2-saturated 0.05 M H_2SO_4 (pH = 1.2) with 1200 rpm stirring. b) Cumulative H_2O_2 concentration, c) cumulative H_2O_2 yield, and d) cumulative H_2O_2 selectivity and Faradaic efficiency during bulk electrolysis.

The electrochemical performance of the treated CCNS (x = 1.2)/CFP did not differ significantly from that of an electrode which was electrochemically conditioned in acid under the electrolysis operating conditions (Figure S16, Figure S17 and Figure S18). This suggests that the acidic solution initially conditions the electrode to be ready for H_2O_2 electrosynthesis, but the electrochemical conditions do not further change the electrode. Additionally, when the electrochemically conditioned CCNS (x = 1.2)/CFP was removed from the electrolyte and immersed in a fresh electrolyte, the second electrolysis run (Figure S19) showed similar

performance to the first run, demonstrating that the electrode remains stable after treatment. Cyclic voltammetry on the electrochemically conditioned catalyst (Figure S20) also suggests the presence of H_2O_2 after the second run on account of the increased reductive current that is indicative of H_2O_2 being further reduced to water, likely limiting the practical performance at higher potentials. In contrast, the reductive current in the first run decreases while the oxidative current increases, suggesting a lack of H_2O_2 buildup and a change in some redox speciation at the electrode (see further discussion later). The full results of the treated CCNS (x = 1.2)/CFP runs are summarized in Table S4. The $CuCo_2S_4$/CFP was also treated and subsequently tested (Figure S21), but was found to be less active than the treated CCNS (x = 1.2)/CFP and did not improve upon further treatment.

Structural Characterization of Acid-Treated Thiospinel Catalysts. The stability of the thiospinel phase through the electrolysis process was confirmed by ex-situ XRD. Spinel phase diffraction peaks appear for both as-prepared and treated CCNS (x = 1.2)/CFP after the 90-minute electrolysis (Figure 4a). This is consistent with the demonstrated stability of a $CuCo_2S_4$ catalyst measured over the same electrolysis time period (Figure S22). Raman spectroscopy further confirmed that the surface structure of the catalyst remains unchanged before and after the electrosynthesis process (Figure 4b and Figure S24). The morphology observed by SEM (Figure S18) does not appear significantly different before and after the treatment and electrolysis process.

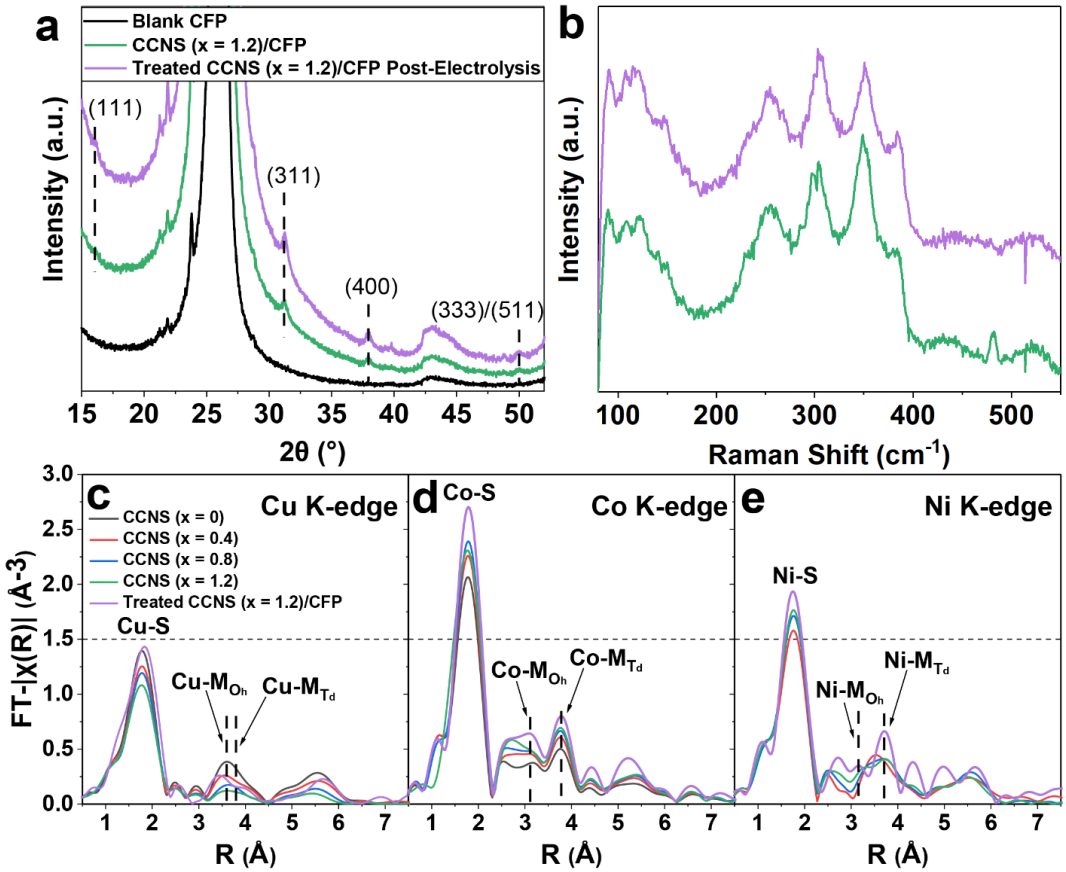

Figure 4. Various CCNS powder samples and treated CCNS/CFP samples characterized ex-situ after-electrolysis by: a) powder X-ray diffraction, b) Raman spectroscopy, c) Cu K-edge EXAFS, d) Co K-edge EXAFS, and e) Ni K-edge EXAFS. The largest diffraction peaks in a) come from carbon paper.

To further probe the mechanism of Ni substitution, ensure that the three metals all exist in a monophasic spinel structure, and check that the metals remain integrated after the treatment procedure, we conducted X-ray absorption spectroscopy (XAS) studies at beamline 10-BM-B of the Advanced Photon Source (see Supporting Information for details). We first measured all four as-synthesized CCNS powder samples with different Ni substitution levels, as well as the treated CCNS/CFP samples. The intensity of the peaks assigned to the Cu to B-site (M_{Oh}) path and the Cu

to A-site (M_{Td}) paths (between 3 Å and 4.5 Å) decrease as the *x*-value increases for CCNS samples while the two peaks become more convoluted (Figure 4c). Meanwhile, the treated CCNS (*x* = 1.2)/CFP has more clearly separated Cu to B-site and Cu to A-site peaks indicating maintained local order and bulk spinel structure after treatment. The Co K-edge EXAFS spectra (Figure 4d) show only significant changes in intensity of the Co to B site and Co to A site peaks, but the uplift of these peaks appears roughly equal, suggesting no significant change in Co's average site environment. The Ni K-edge EXAFS (Figure 4e) suggests a more similar coordination environment to Co than to Cu for the treated CCNS (x = 1.2)/CFP, based on the relative intensities of the scattering paths to octahedral and tetrahedral sites and the larger separation of the major peaks. The pronounced uplift of the Ni-M_{Td} peak for the treated CCNS (x = 1.2)/CFP, without a corresponding increase in the Ni-M_{Oh} peak, could indicate some site rearrangement to compensate for the loss of Cu and maintain charge balance within the structure (more details in Supplementary Note 2). Since the Co K-edge first shell peak has the highest intensity, followed by Ni and then Cu, the Co should also have the highest coordination, followed by Ni and Cu. Furthermore, the Cu EXAFS and Co EXAFS appear consistent with the R-space spectra previously reported for $CuCo_2S_4$.[48] The EXAFS features of a treated CCNS (x = 1.2) sample measured after 90 minutes of electrolysis operation (Figure S25) also showed excellent agreement with the sample measured after treatment without electrolysis operation, further demonstrating the stability of the catalyst in the electrolysis conditions. Finally, to demonstrate the similarity of the structures of the unsupported CCNS and the CFP supported CCNS, we also collected the EXAFS of the untreated CCNS (x = 1.2)/CFP (Figure S25), which showed reasonable agreement with the sample without CFP substrate.

The XANES spectra show minor changes in pre-edge peak positions and the edge position for the Cu K-edge and Ni K-edge before and after the acid treatment (Figure S26 and Figure S27), suggesting some charge transfer as the sites reorganize during the treatment, which was consistent with XPS results (Figure S28). Given that Ni shows apparent mixed oxidation states, Ni(II) and Ni(III) must exist in the structure, and thus a mix of tetrahedral and octahedral coordination is consistent with the stronger octahedral site preference of Ni(II) and weaker octahedral site preference of Ni(III).[35] Moreover, EXAFS fitting results (Figure S29, Table S6-S8, Supplementary Note 3) confirm that the Co coordination number across most samples is significantly higher than the Cu coordination number, and the Ni coordination number lies between Co and Cu, typically indistinguishable between the two within the error of the fit. An increase in the Ni coordination number in CCNS samples with x between 0.4 and 0.8 suggests that the Ni may initially substitute into tetrahedral sites, displacing Cu, only filling octahedral sites in catalysts with higher Ni content. This hypothesis is further supported by the decrease in the convolution of the Ni-T_d peak as the Ni content is increased, resulting in a final treated CCNS (x = 1.2)/CFP structure that more closely resembles the Co EXAFS spectrum for $CuCo_2S_4$, rather than the Cu EXAFS spectrum (see Supplementary Note 2 for more details). Combining the XRD, Raman and XAS results, we can conclude that a single-phase thiospinel structure is maintained in bulk and locally in as-prepared CCNS powders at *x*-values up to 1.2, and the structure is preserved after the acid treatment.

Investigation of the Leached Metal Species during Acid Treatment. To further investigate the mechanism by which the acid treatment modifies the CCNS catalyst, we monitored the metal leaching rates from the catalyst into the treatment solution and in the electrolyte post-electrolysis using ICP-OES (Figure 5a, Table S8, and Table S9). The leaching of Cu during the acid treatment step was faster compared to the leaching rate of the treated CCNS (x = 1.2) under the electrolysis

operation, and both had much faster leaching rates than $CuCo_2S_4$ (Table S10). SEM-EDS, XPS, and ICP-OES elemental composition measurements of the catalyst all confirm a decrease in the formula amount of Cu in treated CCNS (x = 1.2)/CFP to between 0.4 and 0.6, while Co and Ni compositions were not significantly changed (Figure S30 and Table S11-S13). Overall, XPS indicates more metal deficient surfaces for the treated samples, likely due to the kinetics of the leaching process outpacing the reconstruction of metal sites from the bulk replacing sites at the surface. The ~3:4 ratio of metal to sulfur measured for the treated samples by SEM-EDS and ICP-OES further support that the treated CCNS (x = 1.2) sample maintain the spinel phase (Table S11 and S13). We hypothesize that this acid treatment step likely facilitates the rearrangement of the as-synthesized spinel material to a more stable, copper-deficient, complex spinel phase with mixed nickel coordination environments, i.e. $[Cu_{1-\alpha}Ni_{\alpha}]_{tetrahedral}[Co_{2-\beta}Ni_{\beta}]_{octahedral}S_4$, where $\alpha + \beta = x$.

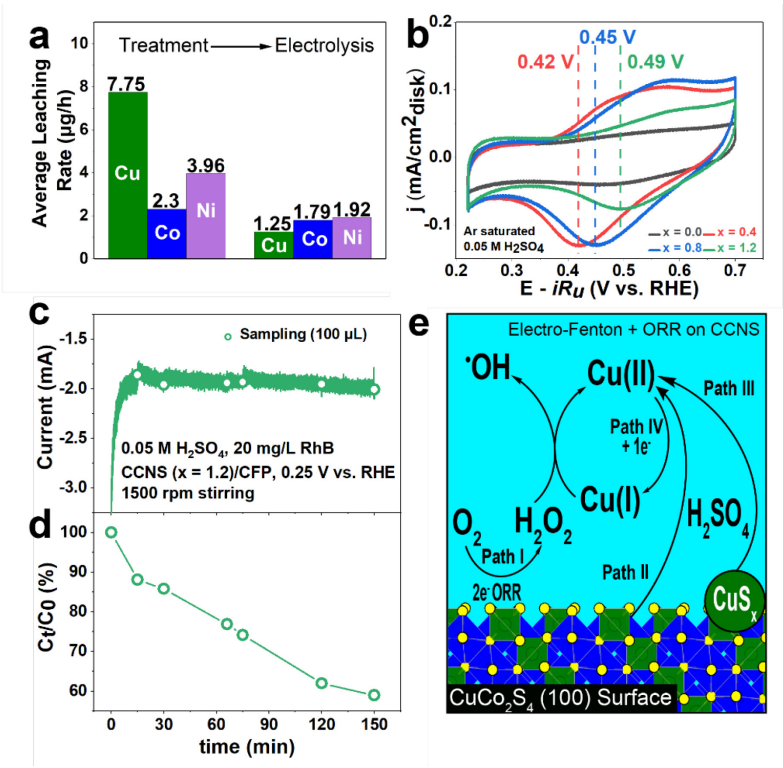

Figure 5. Detection and measurement of Cu leached from the CCNS (x = 1.2) catalyst and its role in electro-Fenton process. a) Metal leaching rates during the acid treatment and during the

electrosynthesis process measured by ICP-OES. b) Cyclic voltammetry of CCNS powders highlighting the shifting Cu(I)/Cu(II) redox feature as the Ni substitution increases. c) Electrolytic Rhodamine B degradation using the Cu-based electro-Fenton process at 0.25 V vs. RHE in 0.05 M H_2SO_4 (pH = 1.2) under 1500 rpm stirring, d) the corresponding concentration profile showing degradation of Rhodamine B over the course of the Fenton electrolysis process. e) Proposed mechanisms of H_2O_2 degradation over the untreated CCNS catalyst where leached Cu^+ ions can catalyze the electro-Fenton process.

The presence of the leached Cu species was further confirmed by cyclic voltammetry in Ar-saturated 0.05 M H_2SO_4 (Figure 5b), which shows that the as-synthesized Ni-containing CCNS samples clearly display a shift in E_{pc} (the potential at the cathodic redox maximum) from 0.42 V vs. RHE for x = 0.4 to 0.49 V vs. RHE for x = 1.2. In contrast, $CuCo_2S_4$ lacks this feature completely. Given the high concentrations of metal ions observed in the treatment solutions of CCNS (x = 1.2)/CFP compared to $CuCo_2S_4$/CFP (Figure 5a and Table S4), it is likely that the leached metal ion(s) led to this redox feature and the shift suggests an increase in the concentration of the redox active species, resulting in Nernstian shift of the redox potential. Co and Ni are ruled out as the redox active species because their characteristic redox features are not in this potential window. This feature is most likely due to the Cu(II) to Cu(I) redox, on account of the greater stability of Cu(II) in solution,[49] which could result in a large Nernstian shift (Figure S31) away from the formal potential of 0.159 V vs. SHE[50] (i.e. 0.230 V vs. RHE at pH = 1.2). The low concentrations of Cu(I) expected due to disproportionation and the low overall concentrations of Cu present during RRDE measurements further support a Cu(II) to Cu(I) redox, and the observed 70 mV shift corresponds to a 10-fold increase in the leached Cu concentration. Some contribution of the Cu(I) to Cu(0) redox is possible, but unlikely due to the higher concentration regime required

for the observed redox potentials and the relative instability of both Cu(I) and Cu(0) in acidic environment. Although the initial oxidation state of Cu in the thiospinel catalysts is expected to be Cu(I),[32, 51] the labile surface Cu(I) could be readily oxidized and leached into solution in acidic conditions. Based on the anodically shifting E_{pc}, the Cu may be more readily leached as the amount of Ni substitution is increased in the CCNS sample. Alternatively, electron transfer between Cu and Ni as more Ni is incorporated, evidenced by shifting oxidation states (Figure S4), could modulate the Cu based redox on the surface instead.

Built-in Electro-Fenton Process via [SJ1] **Leached Copper Species to Generate Hydroxyl Radicals.** Importantly, Cu(I) ions have been previously demonstrated as active Fenton reagents,[52-55] i.e. Cu(I) can react with H_2O_2 to form hydroxyl radicals, which is an even more potent oxidant than H_2O_2 and widely used in environmental applications.[55-57] Therefore, we suspect that H_2O_2 is also produced on the CCNS catalysts that have not been acid treated, but the produced H_2O_2 is quickly converted to hydroxyl radicals by the Cu(I) ions that were leached into the electrolyte. Similar process has been previously reported for Cu_xP catalysts.[53] To confirm this hypothesis, we then ran electrolysis on CCNS/CFP in 0.05 M H_2SO_4 containing a model dye compound commonly used in the studies of electro-Fenton processes,[58] Rhodamine B (Figure 5c). We observed (Figure S32) the degradation of 40% of the dye over the course of 2.5 hours (Figure 5d), which is consistent with the observation in an electro-Fenton process intentionally enabled by adding Fe^{2+} ions.[26]

Based on these evidences, we summarize our proposed mechanism of H_2O_2 degradation in Figure 5e. First, O_2 is reduced to H_2O_2 on the CCNS catalyst via $2e^-$ ORR. Meanwhile, Cu(II) is leached from the oxidation of Cu(I) in the catalyst sample or amorphous Cu impurities termed CuS_x – which has been demonstrated to be relatively inactive for $2e^-$ ORR.[59] The leached Cu(II)

can be subsequently regenerated to Cu(I) on the electrode when a reductive potential is applied, allowing for Cu(I) to subsequently reduce H_2O_2 and generate hydroxyl radicals via a Fenton process, preventing the H_2O_2 concentration from being accumulated unless the soluble Cu species are removed. When the rate of the reduction of H_2O_2 by Cu(I) (which depends on the rate of production of Cu(II) by Path II and Path III and the regeneration of Cu(I) by Path IV) becomes equal to the rate of $2e^-$ ORR (Path I), the maximum concentration of H_2O_2 is reached for that catalyst loading and potential. However, an acid treatment step or the electrolysis process removes the leachable Cu species, therefore H_2O_2 can be successfully accumulated in bulk. If electro-Fenton process and hydroxyl radical generation are desired for water treatment applications, it can be "self-catalyzed" by the built-in Cu(I) species. On the other hand, if concentration built-up of H_2O_2 is desired, the catalyst can be acid-treated before electrolysis.

CONCLUSIONS

We systematically tuned the compositions of $CuCo_{2-x}Ni_xS_4$ thiospinel catalysts by varying the amount of Ni to study the $2e^-$ ORR catalysis. Among the $CuCo_{2-x}Ni_xS_4$ ($0 \leq x \leq 1.2$) samples that maintain a spinel phase, the optimized activity is observed for $CuCo_{2-x}Ni_xS_4$ samples with higher Ni substitution. RRDE measurements show that the $CuCo_{0.8}Ni_{1.2}S_4$ catalyst achieves a ring current density over 1 mA/cm^2_{disk} at 0.25 V vs. RHE while maintaining >60% H_2O_2 selectivity. After an acid treatment procedure, the optimized $CuCo_{0.8}Ni_{1.2}S_4$ catalyst can accumulate up to 84 ppm of H_2O_2 at 0.25 V vs. RHE over the course of 90 minutes, which exceeds that by $CuCo_2S_4$ measured under the same conditions. XRD and Raman confirmed the stability of the spinel phase catalyst after both the acid treatment procedure and electrolysis. XAS results further confirmed that the local coordination environments of all three metals remain the same after the treatment procedure, and that Ni substitution occurs at both tetrahedral and octahedral sites. We found that

the acid treatment procedure preferentially leaches soluble Cu species, which catalyze an electro-Fenton process that consumes the produced H_2O_2 to generate hydroxyl radicals. Thus, the as-synthesized $CuCo_{2-x}Ni_xS_4$ catalyst can be used for electro-Fenton degradation of organic pollutants without need for storage of H_2O_2 or addition of metal Fenton reagents, while the acid treated catalyst can allow for the build-up of H_2O_2 solutions. This study sheds lights onto the mechanisms that lead to composition-tunable intrinsic $2e^-$ ORR selectivity while also highlighting the importance of understanding the phase stability and structural complexity of such catalysts under the operating conditions in order to achieve practical production of H_2O_2. Additionally, these results open the possibility for further improvement of spinel-type catalysts for $2e^-$ ORR by tuning the atomic compositions of different metal sites and provides possible strategies for tuning mixed metal spinel catalysts for selective ORR and subsequent generation of hydroxyl radicals.

AUTHOR INFORMATION

Corresponding Author

***jin@chem.wisc.edu**

The authors declare no competing financial interests.

ASSOCIATED CONTENT

Supporting Information.

The Supporting Information is available free of charge on the ACS Publications website. Experimental methods, additional figures, and tables on materials characterization and electrochemical measurements.

ACKNOWLEDGMENTS

This work is supported by the National Science Foundation (NSF) Grant CHE-1955074. This research used resources of the Advanced Photon Source (APS), a U.S. Department of Energy (DOE) Office of Science User Facility operated for the DOE Office of Science by Argonne National Laboratory under Contract No. DE-AC02-06CH11357. The XAS experiments were conducted at APS Beamline 10-BM-B, and the authors thank Prof. Carlo Segre and Dr. Yujia Ding for their assistance and for data collection on some of the samples. The authors gratefully acknowledge use of facilities and instrumentation at the UW-Madison Wisconsin Centers for Nanoscale Technology (wcnt.wisc.edu) partially supported by the NSF through the Materials Research Science and Engineering Center (DMR-1720415). The authors thank Prof. JR Schmidt and Dr. Aurora N. Janes for helpful discussion and James Lazarcik for assistance with ICP-OES measurements. J.H. also thanks the China Scholarship Council (CSC) for support.

REFERENCES

1. Yang, S.; Verdaguer-Casadevall, A.; Arnarson, L.; Silvioli, L.; Čolić, V.; Frydendal, R.; Rossmeisl, J.; Chorkendorff, I.; Stephens, I. E. L., Toward the Decentralized Electrochemical Production of H_2O_2: A Focus on the Catalysis. *ACS Catal.* **2018,** *8*, 4064-4081.

2. Hydrogen Peroxide Market - Growth, Trends, COVID-19 Impact, and Forecasts (2021 - 2026). https://www.mordorintelligence.com/industry-reports/hydrogen-peroxide-market (accessed 6/22/2021).

3. Jung, E.; Shin, H.; Hooch Antink, W.; Sung, Y. E.; Hyeon, T., Recent Advances in Electrochemical Oxygen Reduction to H_2O_2: Catalyst and Cell Design. *ACS Energy Lett.* **2020,** *5*, 1881-1892.

4. Wang, Y.; Waterhouse, G. I. N.; Shang, L.; Zhang, T., Electrocatalytic Oxygen Reduction to Hydrogen Peroxide: From Homogeneous to Heterogeneous Electrocatalysis. *Adv. Energy Mater.* **2021,** *11*, 2003323.

5. Ciriminna, R.; Albanese, L.; Meneguzzo, F.; Pagliaro, M., Hydrogen Peroxide: A Key Chemical for Today's Sustainable Development. *ChemSusChem* **2016,** *9*, 3374-3381.

6. Campos-Martin, J. M.; Blanco-Brieva, G.; Fierro, J. L. G., Hydrogen Peroxide Synthesis: An Outlook beyond the Anthraquinone Process. *Angew. Chem. Int. Ed.* **2006,** *45*, 6962-6984.

7. Zhou, W.; Meng, X.; Gao, J.; Alshawabkeh, A. N., Hydrogen peroxide generation from O_2 electroreduction for environmental remediation: A state-of-the-art review. *Chemosphere* **2019,** *225*, 588-607.

8. Siahrostami, S.; Villegas, S. J.; Bagherzadeh Mostaghimi, A. H.; Back, S.; Farimani, A. B.; Wang, H.; Persson, K. A.; Montoya, J., A Review on Challenges and Successes in Atomic-Scale Design of Catalysts for Electrochemical Synthesis of Hydrogen Peroxide. *ACS Catal.* **2020,** *10*, 7495-7511.

9. Perry, S. C.; Pangotra, D.; Vieira, L.; Csepei, L.-I.; Sieber, V.; Wang, L.; Ponce de León, C.; Walsh, F. C., Electrochemical synthesis of hydrogen peroxide from water and oxygen. *Nat. Rev. Chem.* **2019,** *3*, 442-458.

10. Siahrostami, S.; Verdaguer-Casadevall, A.; Karamad, M.; Deiana, D.; Malacrida, P.; Wickman, B.; Escudero-Escribano, M.; Paoli, E. A.; Frydendal, R.; Hansen, T. W.; Chorkendorff, I.; Stephens, I. E. L.; Rossmeisl, J., Enabling direct H_2O_2 production through rational electrocatalyst design. *Nat. Mater.* **2013,** *12*, 1137-1143.

11. Verdaguer-Casadevall, A.; Deiana, D.; Karamad, M.; Siahrostami, S.; Malacrida, P.; Hansen, T. W.; Rossmeisl, J.; Chorkendorff, I.; Stephens, I. E. L., Trends in the electrochemical

synthesis of H_2O_2: Enhancing activity and selectivity by electrocatalytic site engineering. *Nano Lett.* **2014,** *14*, 1603-1608.

12. Lu, Z.; Chen, G.; Siahrostami, S.; Chen, Z.; Liu, K.; Xie, J.; Liao, L.; Wu, T.; Lin, D.; Liu, Y.; Jaramillo, T. F.; Nørskov, J. K.; Cui, Y., High-efficiency oxygen reduction to hydrogen peroxide catalysed by oxidized carbon materials. *Nat. Catal.* **2018,** *1*, 156-162.

13. Gong, K.; Du, F.; Xia, Z.; Durstock, M.; Dai, L., Nitrogen-doped carbon nanotube arrays with high electrocatalytic activity for oxygen reduction. *Science* **2009,** *323*, 760-764.

14. Kim, H. W.; Ross, M. B.; Kornienko, N.; Zhang, L.; Guo, J.; Yang, P.; McCloskey, B. D., Efficient hydrogen peroxide generation using reduced graphene oxide-based oxygen reduction electrocatalysts. *Nat. Catal.* **2018,** *1*, 282-290.

15. Sun, Y.; Sinev, I.; Ju, W.; Bergmann, A.; Dresp, S.; Kühl, S.; Spöri, C.; Schmies, H.; Wang, H.; Bernsmeier, D.; Paul, B.; Schmack, R.; Kraehnert, R.; Roldan Cuenya, B.; Strasser, P., Efficient Electrochemical Hydrogen Peroxide Production from Molecular Oxygen on Nitrogen-Doped Mesoporous Carbon Catalysts. *ACS Catal.* **2018,** *8*, 2844-2856.

16. Qiang, Z.; Chang, J. H.; Huang, C. P., Electrochemical generation of hydrogen peroxide from dissolved oxygen in acidic solutions. *Water Res.* **2002,** *36*, 85-94.

17. Gao, J.; Yang, H. b.; Huang, X.; Hung, S.-F.; Cai, W.; Jia, C.; Miao, S.; Chen, H. M.; Yang, X.; Huang, Y.; Zhang, T.; Liu, B., Enabling Direct H_2O_2 Production in Acidic Media through Rational Design of Transition Metal Single Atom Catalyst. *Chem* **2020,** *6*, 658-674.

18. Jung, E.; Shin, H.; Lee, B. H.; Efremov, V.; Lee, S.; Lee, H. S.; Kim, J.; Hooch Antink, W.; Park, S.; Lee, K. S.; Cho, S. P.; Yoo, J. S.; Sung, Y. E.; Hyeon, T., Atomic-level tuning of Co–N–C catalyst for high-performance electrochemical H_2O_2 production. *Nat. Mater.* **2020,** *19*, 436-442.

19. Sun, Y.; Silvioli, L.; Sahraie, N. R.; Ju, W.; Li, J.; Zitolo, A.; Li, S.; Bagger, A.; Arnarson, L.; Wang, X.; Moeller, T.; Bernsmeier, D.; Rossmeisl, J.; Jaouen, F.; Strasser, P., Activity–Selectivity Trends in the Electrochemical Production of Hydrogen Peroxide over Single-Site Metal–Nitrogen–Carbon Catalysts. *J. Am. Chem. Soc.* **2019,** *141*, 12372-12381.

20. Guo, X.; Lin, S.; Gu, J.; Zhang, S.; Chen, Z.; Huang, S., Simultaneously Achieving High Activity and Selectivity towards Two-Electron O_2 Electroreduction: the Power of Single-Atom Catalysts. *ACS Catal.* **2019,** *9*, 11042-11054.

21. Jiang, K.; Back, S.; Akey, A. J.; Xia, C.; Hu, Y.; Liang, W.; Schaak, D.; Stavitski, E.; Nørskov, J. K.; Siahrostami, S.; Wang, H., Highly selective oxygen reduction to hydrogen peroxide on transition metal single atom coordination. *Nat. Commun.* **2019,** *10,* 3997.

22. Tang, L. C., Haijing Li, Laiquan Li, Yan Jiao, Yao Zheng, Haolan Xu, Kenneth Davey, Shi-Zhang Qiao, Tailoring Acidic Oxygen Reduction Selectivity on Single-Atom Catalysts via Modification of First and Second Coordination Spheres. *J. Am. Chem. Soc.* **2021,** *143*, 7819-7827.

23. Lian, Y.; Yang, W.; Zhang, C.; Sun, H.; Deng, Z.; Xu, W.; Song, L.; Ouyang, Z.; Wang, Z.; Guo, J.; Peng, Y., Unpaired 3d Electrons on Atomically Dispersed Cobalt Centres in Coordination Polymers Regulate both Oxygen Reduction Reaction (ORR) Activity and Selectivity for Use in Zinc–Air Batteries. *Angew. Chem. Int. Ed.* **2020,** *59*, 286-294.

24. Sheng, H.; Hermes, E. D.; Yang, X.; Ying, D.; Janes, A. N.; Li, W.; Schmidt, J. R.; Jin, S., Electrocatalytic Production of H_2O_2 by Selective Oxygen Reduction Using Earth-Abundant Cobalt Pyrite (CoS_2). *ACS Catal.* **2019,** *9*, 8433-8442.

25. Zhao, W. W.; Bothra, P.; Lu, Z.; Li, Y.; Mei, L. P.; Liu, K.; Zhao, Z.; Chen, G.; Back, S.; Siahrostami, S.; Kulkarni, A.; Nørskov, J. K.; Bajdich, M.; Cui, Y., Improved Oxygen

Reduction Reaction Activity of Nanostructured CoS_2 through Electrochemical Tuning. *ACS Appl. Energy Mater.* **2019,** *2*, 8605-8614.

26. Sheng, H.; Janes, A. N.; Ross, R. D.; Kaiman, D.; Huang, J.; Song, B.; Schmidt, J. R.; Jin, S., Stable and selective electrosynthesis of hydrogen peroxide and the electro-Fenton process on $CoSe_2$ polymorph catalysts. *Energy and Environ. Sci.* **2020,** *13*, 4189-4203.

27. Liang, J.; Wang, Y.; Liu, Q.; Luo, Y.; Li, T.; Zhao, H.; Lu, S.; Zhang, F.; Asiri, A. M.; Liu, F.; Ma, D.; Sun, X., Electrocatalytic hydrogen peroxide production in acidic media enabled by NiS_2 nanosheets. *J. Mater. Chem. A* **2021,** *9*, 6117-6122.

28. Li, H.; Wen, P.; Itanze, D. S.; Hood, Z. D.; Adhikari, S.; Lu, C.; Ma, X.; Dun, C.; Jiang, L.; Carroll, D. L.; Qiu, Y.; Geyer, S. M., Scalable neutral H_2O_2 electrosynthesis by platinum diphosphide nanocrystals by regulating oxygen reduction reaction pathways. *Nat. Commun.* **2020,** *11*, 3928.

29. Zhao, Q.; Yan, Z.; Chen, C.; Chen, J., Spinels: Controlled Preparation, Oxygen Reduction/Evolution Reaction Application, and beyond. *Chem. Rev.* **2017,** *117*, 10121-10211.

30. Bhargava, A.; Chen, C. Y.; Finkelstein, K. D.; Ward, M. J.; Robinson, R. D., X-ray emission spectroscopy: An effective route to extract site occupation of cations. *Phys. Chem. Chem. Phys.* **2018,** *20*, 28990-29000.

31. Moris, S.; Valencia-Gálvez, P.; Mejía-López, J.; Peña, O.; Barahona, P.; Galdámez, A., $(Cu)_{tet}(Cr_{2-x}Sn_x)_{oct}S_{4-y}Se_y$ Spinels: Crystal Structure, Density Functional Theory Calculations, and Magnetic Behavior. *Inorg. Chem.* **2019,** *58*, 13945-13952.

32. Bosi, F.; Biagioni, C.; Pasero, M., Nomenclature and classification of the spinel supergroup. *Eur. J. Mineral.* **2019,** *31*, 183-192.

33. Biagioni, C.; Pasero, M., The systematics of the spinel-type minerals: An overview. *Am. Mineral.* **2014,** *99*, 1254-1264.

34. Waerenborgh, J. C.; Figueiredo, M. O.; Cabral, J. M. P.; Pereira, L. C. J., Temperature and Composition Dependence of the Cation Distribution in Synthetic $ZnFe_yAl_{2-y}O_4$ ($0 \leqslant y \leqslant 1$) Spinels. *J. Solid State Chem.* **1994,** *111*, 300-309.

35. Liu, Y.; Ying, Y.; Fei, L.; Liu, Y.; Hu, Q.; Zhang, G.; Pang, S. Y.; Lu, W.; Mak, C. L.; Luo, X.; Zhou, L.; Wei, M.; Huang, H., Valence Engineering via Selective Atomic Substitution on Tetrahedral Sites in Spinel Oxide for Highly Enhanced Oxygen Evolution Catalysis. *J. Am. Chem. Soc.* **2019,** *141*, 8136-8145.

36. Wu, T.; Sun, S.; Song, J.; Xi, S.; Du, Y.; Chen, B.; Sasangka, W. A.; Liao, H.; Gan, C. L.; Scherer, G. G.; Zeng, L.; Wang, H.; Li, H.; Grimaud, A.; Xu, Z. J., Iron-facilitated dynamic active-site generation on spinel $CoAl_2O_4$ with self-termination of surface reconstruction for water oxidation. *Nat. Catal.* **2019,** *2*, 763-772.

37. Duan, Y.; Sun, S.; Sun, Y.; Xi, S.; Chi, X.; Zhang, Q.; Ren, X.; Wang, J.; Ong, S. J. H.; Du, Y.; Gu, L.; Grimaud, A.; Xu, Z. J., Mastering Surface Reconstruction of Metastable Spinel Oxides for Better Water Oxidation. *Adv. Mater.* **2019,** *31*, 1807898.

38. Zhao, S.; Wang, Y.; Zhang, Q.; Li, Y.; Gu, L.; Dai, Z.; Liu, S.; Lan, Y. Q.; Han, M.; Bao, J., Two-dimensional nanostructures of non-layered ternary thiospinels and their bifunctional electrocatalytic properties for oxygen reduction and evolution: The case of $CuCo_2S_4$ nanosheets. *Inorg. Chem. Front.* **2016,** *3*, 1501-1509.

39. Shannon, R. D., Revised Effective Ionic Radii and Systematic Studies of Interatomic Distances in Halides and Chalcogenides. *Acta Crystallogr.* **1976,** *32*, 751-767.

40. Craig, J. R.; Carpenter, A. B., Fletcherite, $Cu(Ni, Co)_2S_4$, a new thiospinel from the Viburnum Trend (New Lead Belt), Missouri. *Econ. Geol.* **1977,** *72*, 480-486.

41. Ostwald, J., Fletcherite and its genesis in the Kalgoorlie area, Western Australia. *Jb. Miner. Mh.* **1985,** *1*, 35-44.

42. Smirnov, S. G.; Kesler, Y. A., Electronic-Structure and Evolution of Linnaeite Group Thiospinels. *Dokl. Phys. Chem.* **1990,** *311*, 331-335.

43. Wei, C.; Feng, Z.; Scherer, G. G.; Barber, J.; Shao-Horn, Y.; Xu, Z. J., Cations in Octahedral Sites: A Descriptor for Oxygen Electrocatalysis on Transition-Metal Spinels. *Adv. Mater.* **2017,** *29*, 1606800.

44. Du, X.; Zhang, X.; Yang, Z.; Gong, Y., Water Oxidation Catalysis Beginning with $CuCo_2S_4$: Investigation of the True Electrochemically Driven Catalyst. *Chem.: Asian J.* **2018,** *13*, 266-270.

45. Vijayakumar, S.; Lee, S. H.; Ryu, K. S., Hierarchical $CuCo_2O_4$ nanobelts as a supercapacitor electrode with high areal and specific capacitance. *Electrochim. Acta* **2015,** *182*, 979-986.

46. Chauhan, M.; Reddy, K. P.; Gopinath, C. S.; Deka, S., Copper Cobalt Sulfide Nanosheets Realizing a Promising Electrocatalytic Oxygen Evolution Reaction. *ACS Catal.* **2017,** *7*, 5871-5879.

47. Bonakdarpour, A.; Lefevre, M.; Yang, R.; Jaouen, F.; Dahn, T.; Dodelet, J. P.; Dahn, J. R., Impact of loading in RRDE experiments on Fe-N-C catalysts: Two- or four-electron oxygen reduction? *Electrochem. Solid-State Lett.* **2008,** *11*, 105-108.

48. Li, Y.; Yin, J.; An, L.; Lu, M.; Sun, K.; Zhao, Y. Q.; Cheng, F.; Xi, P., Metallic $CuCo_2S_4$ nanosheets of atomic thickness as efficient bifunctional electrocatalysts for portable, flexible Zn-air batteries. *Nanoscale* **2018,** *10*, 6581-6588.

49. Johnson, D. K.; Stevenson, M. J.; Almadidy, Z. A.; Jenkins, S. E.; Wilcox, D. E.; Grossoehme, N. E., Stabilization of Cu(I) for binding and calorimetric measurements in aqueous solution. *Dalton Trans.* **2015,** *44*, 16494-16505.

50. Bard, A. J.; Parsons, R.; Jordan, J., *Standard Potentials in Aqueous Solution*. CRC Press: 1985; pp 292.

51. Pattrick, R. A. D.; Coker, V. S.; Pearce, C. I.; Telling, N. D.; van der Laan, G., The oxidation state of copper and cobalt in carrollite, $CuCo_2S_4$. *Can. Mineral.* **2008,** *46*, 1317-1322.

52. Lee, H.; Lee, H. J.; Seo, J.; Kim, H. E.; Shin, Y. K.; Kim, J. H.; Lee, C., Activation of Oxygen and Hydrogen Peroxide by Copper(II) Coupled with Hydroxylamine for Oxidation of Organic Contaminants. *Environ. Sci. Technol.* **2016,** *50*, 8231-8238.

53. Kim, H.; Lim, J.; Lee, S.; Kim, H. H.; Lee, C.; Lee, J.; Choi, W., Spontaneous Generation of H_2O_2 and Hydroxyl Radical through O2 Reduction on Copper Phosphide under Ambient Aqueous Condition. *Environ. Sci. Technol.* **2019,** *53*, 2918-2925.

54. Lee, H.; Lee, H. J.; Sedlak, D. L.; Lee, C., pH-Dependent reactivity of oxidants formed by iron and copper-catalyzed decomposition of hydrogen peroxide. *Chemosphere* **2013,** *92*, 652-658.

55. Brillas, E.; Garcia-Segura, S., Benchmarking recent advances and innovative technology approaches of Fenton, photo-Fenton, electro-Fenton, and related processes: A review on the relevance of phenol as model molecule. *Sep. Purif. Technol.* **2020,** *237*, 116337.

56. Brillas, E.; Sirés, I.; Oturan, M. A., Electro-fenton process and related electrochemical technologies based on fenton's reaction chemistry. *Chem. Rev.* **2009,** *109*, 6570-6631.

57. Pignatello, J. J.; Oliveros, E.; MacKay, A., Advanced oxidation processes for organic contaminant destruction based on the fenton reaction and related chemistry. *Crit. Rev. Environ. Sci. Technol.* **2006,** *36*, 1-84.

58. Yuan, S.; Fan, Y.; Zhang, Y.; Tong, M.; Liao, P., Pd-Catalytic In Situ Generation of H_2O_2 from H_2 and O_2 Produced by Water Electrolysis for the Efficient Electro-Fenton Degradation of Rhodamine B. *Environ. Sci. Technol.* **2011,** *45*, 8514-8520.

59. Shen, R.; Chen, W.; Peng, Q.; Lu, S.; Zheng, L.; Cao, X.; Wang, Y.; Zhu, W.; Zhang, J.; Zhuang, Z.; Chen, C.; Wang, D.; Li, Y., High-Concentration Single Atomic Pt Sites on Hollow CuS_x for Selective O_2 Reduction to H_2O_2 in Acid Solution. *Chem* **2019,** *5*, 2099-2110.

TOC Graph

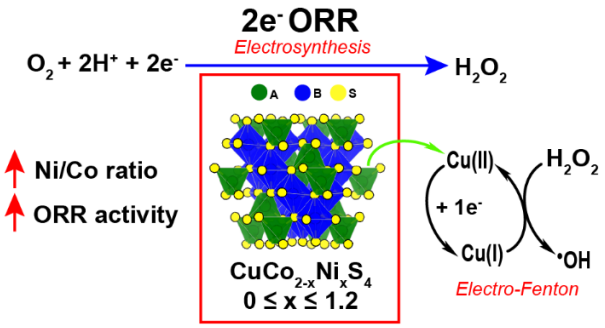
2e- ORR
Electrosynthesis
O2 + 2H+ + 2e-
H2O2
A
B
S
Ni/Co ratio
ORR activity
CuCo2-xNixS4
0 ≤ x ≤ 1.2
Cu(II)
+ 1e-
Cu(I)
H2O2
•OH
Electro-Fenton